

Separation control and drag reduction using roughness elements

N. Beratlis

Department of Mechanical Engineering
Arizona State University
Tempe, AZ
nikos.beratlis@gmail.com

K. Squires

Department of Mechanical Engineering
Arizona State University
Tempe, AZ
squires@asu.edu

E. Balaras

Department of Mechanical Engineering
George Washington University
Washington, DC
balaras@gwu.edu

ABSTRACT

In the present work the effects of different types of roughness elements on flow separation over a curved boundary is investigated by means of direct numerical simulations. The geometry and boundary conditions are such that the basic physics of the flow over bluff bodies are represented. Two types of roughness elements are considered, dimples and spherical beads. The Reynolds number, Re_h , based on the freestream velocity and height, varied from 3,000 to 30,000. The results are in good qualitative agreement with results for flow over bluff bodies with surface roughness. In particular, the roughness elements are very effective in causing transition of the boundary layer at a much lower Reynolds numbers when compared to a smooth surface. For the spherical beads the drag coefficient exhibits a minimum and quickly rises as the Reynolds number increases. For the dimples the minimum drag coefficient remains constant and independent of the Reynolds number within the range considered in this study. The reason for this different behavior lies in the way the boundary layer grows between the two different roughness elements. For the spherical beads the transition shifts upstream and moves toward the stagnation point on the front of the bump as the Reynolds number increases. An earlier transition means the boundary layer starts growing thicker earlier and has less momentum to overcome the adverse pressure gradient. As a result the separation point moves upstream too giving rise to increased drag. In contrast the transition and separation points are weakly dependent on the Reynolds number for the case of the dimples.

INTRODUCTION

Various roughness elements have been long used to reduce drag on both bluff and streamlined bodies. Figure 1 shows a plot of the drag coefficient versus Reynolds number for spheres with smooth or roughened surfaces. For the smooth sphere the drag coefficient begins to drop around a Reynolds number $Re \sim 400,000$, (where Re is based on the free stream velocity U , diameter of the sphere D). The drag coefficient reaches a minimum value of 0.08 after which it starts to augment as the Reynolds number increases. This phenomena is termed the drag crisis and is associated with transition of the boundary layers from laminar to turbulent. When roughness elements are used the drag crisis can be dramatically accelerated and the drag coefficient can be lowered compared to that of a smooth sphere at the same Reynolds number. However the type of roughness elements can play a big role on the magnitude and behavior of the drag in the post-critical regime. For example, Achenbach

(1974) showed that the drag crisis on a sphere can be significantly accelerated by using small glass beads glued to its surface or by roughening the surface with sandpaper. As the size of the roughness elements increases the critical Reynolds number is reduced. However the minimum drag coefficient can not be maintained and it rises very quickly as the Reynolds number is increased. Güven *et al.* (1980) and Achenbach (1971) conducted wind tunnel experiments on cylinders with sandpaper wrapped around their perimeter and they found that this kind of distributed roughness causes a much quicker thickening of the boundary layer with increasing Reynolds number. In particular, as the Reynolds number increases both the transition and separation point move upstream resulting in an increase in drag. Dimples are another form of roughness elements commonly employed to reduce drag. In contrary to random or distributed roughness dimples can maintain the low drag in the post-critical region. Bearman & Harvey (1976) conducted wind tunnel tests on stationary and spinning golf balls and found out that the shape of the dimples can affect the minimum drag of the golf ball. In particular, golf ball with hexagonal dimples had a lower drag coefficient than golf balls with spherical dimples. In both cases the drag coefficient for $Re = 80000 - 240000$ remained approximately constant. Choi *et al.* (2006) carried out wind tunnel experiments on a dimpled sphere and showed that dimples cause local flow separation and trigger the shear layer instability along the separating shear layer, resulting in the generation of large turbulence intensity. AOKI *et al.* (2012) conducted experiments with dimpled spheres where they varied the depth of the dimples. They found that as the dimple depth increased the critical Reynolds number decreased. However, the separation point shifted to the upstream side and the drag coefficient became larger in the super-critical Reynolds number region. Flow visualization using an oil film method showed that as the dimple depth increased flow separation inside dimples moves upstream. It is not clear though how the transition point is affected by dimple depth. Finally Aoki *et al.* (2003) showed that as the number of dimples on a sphere increased the critical Reynolds number decreased and the minimum drag coefficient increased. Using an oil film method they showed that the separation point in the super critical regime was delayed.

The present work presents a series of direct numerical simulations (DNS) of flow over a curved boundary. The geometry and boundary conditions are such that the basic physics of the flow over bluff bodies are represented. The surface is either smooth, covered with dimples or is roughened using spherical beads.

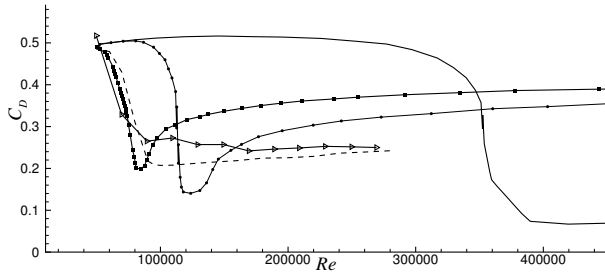


Figure 1. Plot of drag coefficient C_D versus Reynolds number for a stationary smooth sphere and various golf balls. Lines represent: —; smooth sphere, - - -; dimpled sphere, - \triangleright -; dimpled sphere - \cdot -; rough sphere.

PROBLEM SETUP

The three geometries used in this study are shown in Figure 2. All surfaces have a predominantly cylindrical shape. The smooth bump shown in Figure 2a has a maximum height, $h = 15d$ and a length of $L = 80d$ (d is the dimple depth defined below), and is part of a cylinder with radius of 60.83. The geometry shown in Figure 2b has the same basic shape but it contains 7 rows of spherical dimples. Each row is staggered with respect to the previous one. The spherical dimples have a maximum depth of $d = 1$ and an inscribed diameter of $10d$. The geometry shown in Figure 2c has a rough surface created by placing small spheres with diameter of $1d$ on the top. In total there are 77 staggered rows of spheres covering the entire surface of the bump. The spheres are placed $1.22d$ apart in the spanwise direction. Note that only 90% of the sphere protrudes into the flow, while the remaining part is immersed in the bump. The resulting surface topology is very similar to the one used by Achenbach (1974), and will enable qualitative comparisons with our computations.

An outline of the computational domain is shown in Figure 3. The streamwise, wall-normal and spanwise directions are noted by x , y and z respectively. The bump extends from $-40d$ to $40d$ and from 0 to $15d$ in the streamwise and wall-normal directions respectively. The computational domain is a box with dimensions $260d \times 120d \times 11d$. The bump which is not aligned with the grid is introduced using an immersed boundary formulation. At the inlet a uniform velocity profile is specified. From the inlet to the front of the bump there is a slip-wall. This prevents the boundary layer from growing in front of the bump. A slip wall is specified at the top and at the outflow boundary a convective boundary condition is used. The Reynolds number based on the freestream velocity and the height of the bump was varied from $7500 < Re_h < 30000$.

The simulations are carried out using an in-house finite-difference Navier-Stokes solver. The governing equations are discretized on a structured grid in Cartesian coordinates. The boundary conditions on the curved surface, which is not aligned with the grid lines, are imposed using an immersed-boundary formulation Yang & Balaras (2006). An exact, semi-implicit, projection method is used for the time advancement. All terms are treated explicitly using the Runge-Kutta third order scheme, except for the viscous and convective terms in the wall-normal direction which are treated implicitly using a second order Crank-Nicholson scheme. All spatial derivatives are discretized using second-order central-differences on a staggered grid. The code is parallelized using a classical domain decomposition approach. Details on the overall formulation together with a comprehensive validation study can be found in Balaras (2004); Balaras & Yang (2005); Yang & Balaras (2006).

A grid refinement study was performed for the case of the dim-

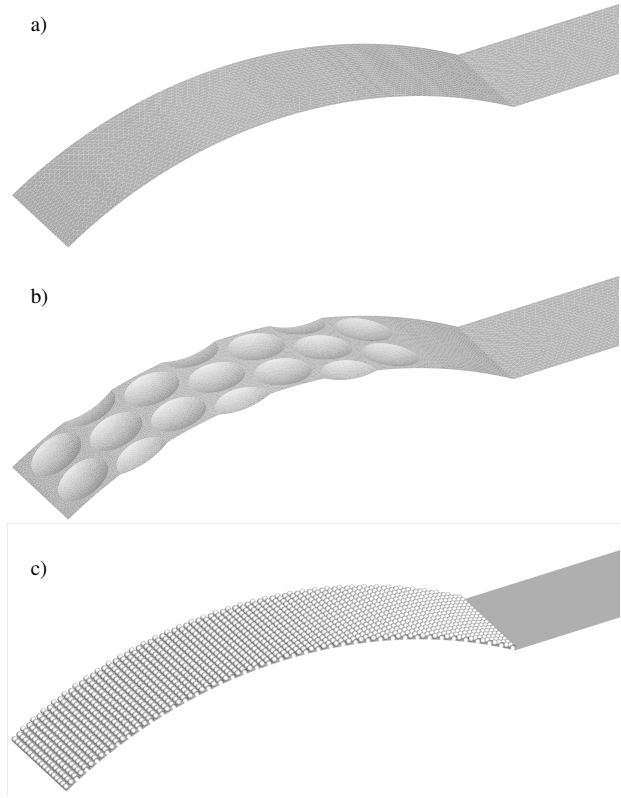


Figure 2. Geometries used in this study a) smooth bump, b) dimpled bump, and c) rough bump

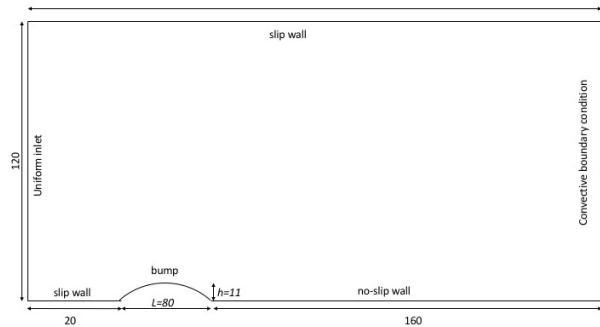


Figure 3. Outline of the computational domain and boundary conditions.

pled geometry at the highest Reynolds, $Re_h = 30000$. Three grid resolutions were considered. The coarse grid contains $947 \times 102 \times 952$ points in x, y , and z directions respectively. The medium grid contains $1421 \times 152 \times 1452$ in x, y , and z respectively, which is a 50% grid refinement in each direction. The fine grid contains $1900 \times 1395 \times 200$ points, out of which, $1300 \times 1100 \times 200$ points are uniformly distributed in a box encompassing the bump. The grid resolution on the fine grid is twice that on the coarse grid in each direction. Figure 4 shows plots of the pressure coefficient, C_p , and the skin friction coefficient, C_f , for the three grids. The coefficients are averaged over time and the spanwise direction. The skin friction coefficient for the coarse grid is underestimated and there is a slightly different behavior of the pressure at the back of the bump. However the medium and fine grids are in very close agreement with each other indicating that the solution is grid independent. All the results below are from the fine grid.

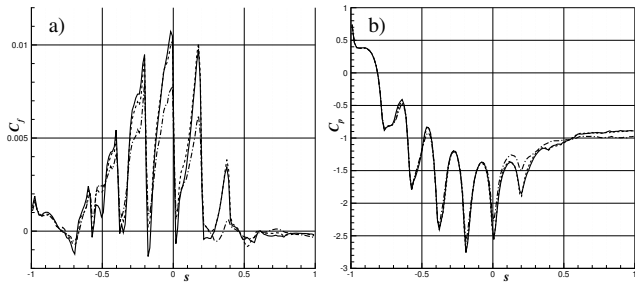


Figure 4. Plots of a) the skin friction coefficient C_f and b) the pressure coefficient C_p for the case of the dimpled bump at $Re_h = 30000$ and for three different grids. Lines represent - - -; coarse, - - -; medium, — fine.

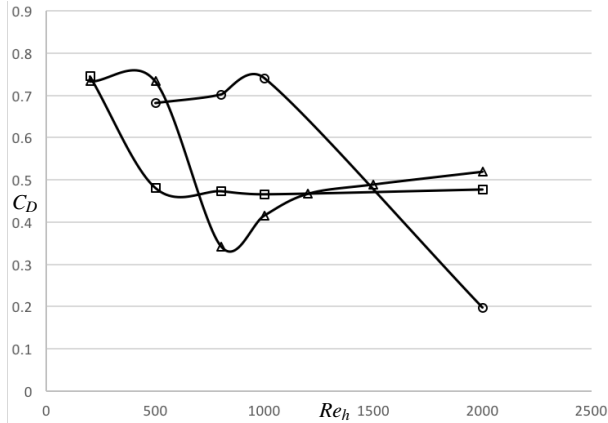


Figure 5. Plot of the drag coefficient versus Reynolds number. Symbol represent: - o -; smooth bump, - □ -; dimpled bump, - ▷ -; rough bump

RESULTS

We start the discussion by looking at the behavior of the drag coefficient for the three different surfaces (see Figure 5). For the smooth surface the drag coefficient is $C_d = 0.47$ at $Re_h = 11000$ and decreases to $C_d = 0.35$ at $Re_h = 22000$ marking the onset of the drag crisis. For the rough surface the drag coefficient is initially, $C_d = 0.5$ at $Re_h = 5500$. The presence of the small spheres on the surface increase the wetted area and result in higher drag than the smooth case. However at $Re_h = 9900$ the drag coefficient drops to $C_d = 0.34$ indicating that the boundary layer transitions from laminar to turbulent. Further increase in the Reynolds number result in an increase of the drag. This behavior is qualitatively similar to the one observed on spheres and cylinders with surface roughness. For the case of the dimpled surface the drag coefficient drops to a value of $C_d = 0.3$ at $Re_h = 11000$ and remains low at higher Reynolds numbers. This is a confirmation that the present configuration exhibits the same trends observed on generic bluff bodies and is suitable for studying the effects of surface roughness on flow separation.

Smooth surface

First we present some results for the flow over the smooth surface. Figure 6 shows contours of the spanwise vorticity, ω_z , at a spanwise plane and for two Reynolds numbers in the subcritical regime. The boundary layer remains laminar over the surface and it separates near the top. After separation the shear layer becomes unstable and rolls-up into a vortex sheet. The vortex sheet breaks down into smaller vortices creating a turbulent wake. As the Reynolds

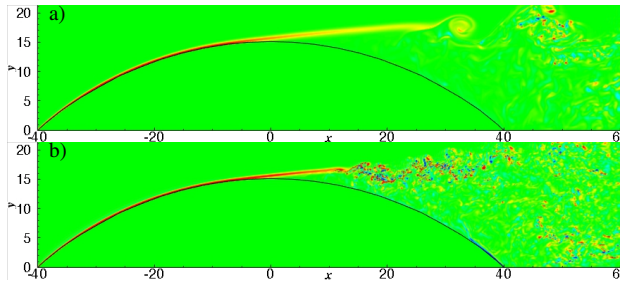


Figure 6. Contours of the instantaneous span wise vorticity ω_z at a span wise plane for the case of the smooth bump. a) $Re_h = 7500$ and b) $Re_h = 15000$.

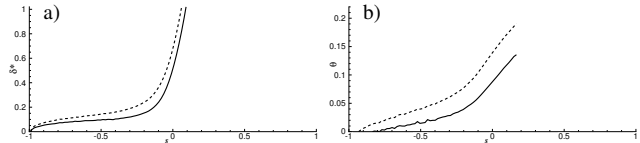


Figure 7. Boundary layer statistics averaged over time and span for the case of the smooth bump. a) Displacement thickness δ^* and b) momentum thickness θ . Lines represent - - $Re_h = 7500$ and - $Re_h = 15000$.

number increases the shear layers instability moves closer to the separation point and the vortical structures become smaller. Figure 7 shows the evolution of the boundary layer over the surface. The boundary layer thickness, δ , and momentum thickness, θ , are plotted versus the arc-length, s , which varies from -1 at the front, 0 at the top, to 1 at the trailing edge. It is clear that as the Reynolds number increases the boundary layer becomes thinner. However the separation point as shown in Figure 8 doesn't change. In both cases the boundary layer separates at approximately $s = -0.07$. As a result the pressure coefficient, C_p , and consequently the drag remain constant. As the Reynolds number increases even further (not shown here), the shear layer instability moves closer to the surface and the flow reattaches. This is accompanied by a gradual drop in the drag coefficient (see Figure 5), which represents the onset of the drag crisis.

Rough surface

For the rough surface the boundary layer transitions earlier. Figure 9 shows contours of the instantaneous spanwise vorticity on a spanwise plane passing through the middle of the geometry, for two Reynolds numbers: $Re_h = 12000$ corresponding to the minimum drag, and $Re_h = 30000$. In both cases the flow is in the post-critical regime. For the $Re_h = 12000$ case the boundary layer at the front of the bump remains laminar. Local shear layers form over individual roughness elements but remain stable. Towards the top however, the shear layers become unstable giving birth to vortical structures that populate the near wall flow. These structures energize the flow and separation is delayed compared to the smooth case. For the $Re_h = 30000$ small vortical structures are present very close to the stagnation point at the front indicating that transition occurs earlier. The flow also separates earlier compared to the $Re_h = 12000$ case.

We next look on the boundary layer growth over the rough surface. Figure 10 shows profiles of the tangential velocity, U_t , at various locations for both Reynolds numbers. The profiles are averaged over time and the spanwise direction. Up to a distance of $0.9d$ away from the surface the averaging includes areas of both solid and fluid

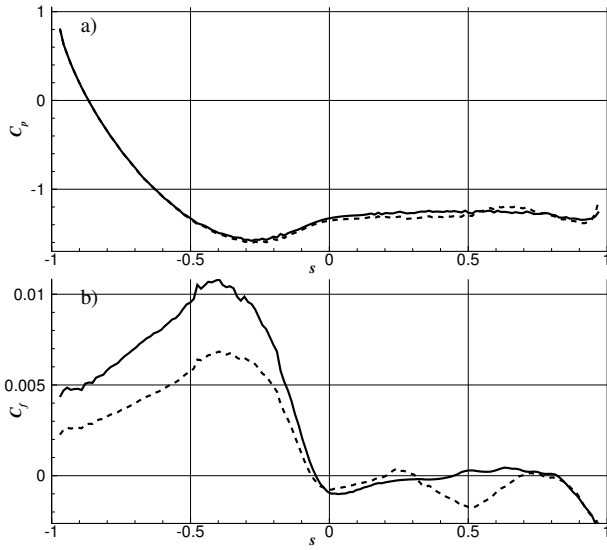


Figure 8. Plot of a) C_D and b) C_f versus stream wise coordinate for the case of the smooth bump. Lines represent - - $Re_h = 7500$ and - $Re_h = 15000$.

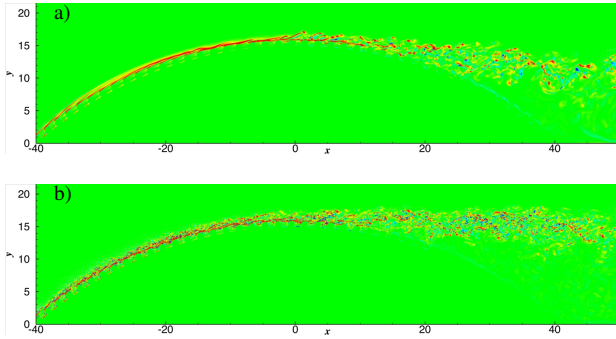


Figure 9. Contours of the instantaneous span wise vorticity for the case of the rough bump at a plane passing through the middle of the bump. a) $Re = 12000$ and b) $Re = 30000$

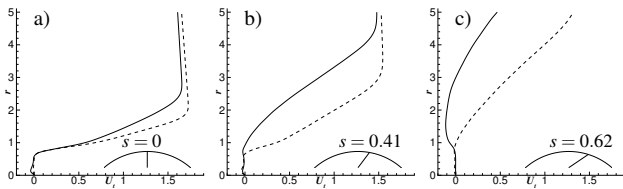


Figure 10. Profiles of the tangential velocity for rough bump at different locations: a) $s = 0.0$, b) $s = 0.41$ and c) $s = 0.62$. Lines represent: —; $Re = 12000$, - - - $Re = 30000$.

pockets. At a distance greater than $0.9d$ every point is a fluid point. The profiles reveal that for the higher Reynolds number there is a momentum deficit in the boundary layer already at $s = 0$, which is at the very top of the curved surface (s is a non-dimensional arch-length ranging from $-1 < s < 1$ as shown in Figure 11). The momentum deficit persists further downstream. As a result the boundary layer separates around $s = 0.51$ for the $Re = 30000$ case and around $s = 0.83$ for the $Re = 12000$ case. This is a significant delay in the separation of the boundary layer.

Figure 11 shows the turbulent kinetic energy, q , averaged over time and the spanwise direction along an arc passing 0.5 units above

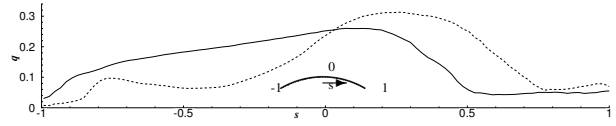


Figure 11. Plot of the average turbulent kinetic energy along an arc line passing 0.5 above the rough wall. Lines represent: - - -; $Re = 12000$, — $Re = 30000$.

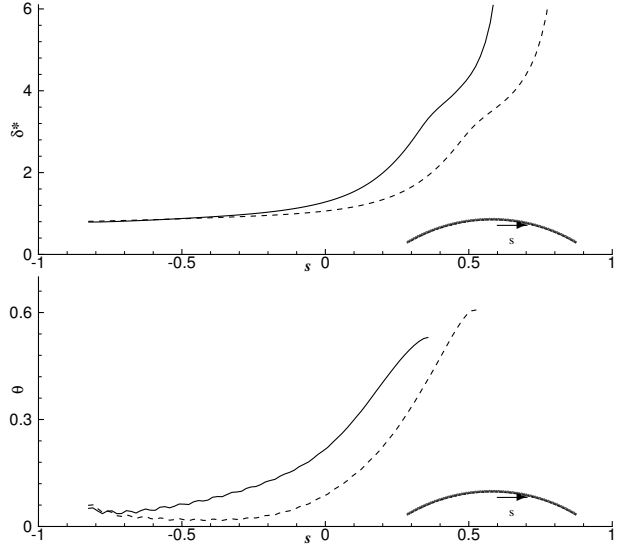


Figure 12. Plot of a) displacement thickness δ^* and b) momentum thickness θ along the rough bump. Lines represent: —; $Re_h = 12000$, - - - $Re_h = 30000$.

the rough wall. The plot clearly illustrates that as the Reynolds number increases the transition point moves slightly upstream. For the $Re_h = 30000$ case the levels of q increase quickly at the front, while for the $Re_h = 12000$ case the levels of q are negligible at the stagnation point and become higher near the top. Consequently the momentum transport across the boundary layer occurs earlier for $Re_h = 30000$ and the boundary layer thickens faster and separates earlier. This is clearly reflected in the evolution of the displacement and momentum thickness shown in Figure 12.

Dimpled surface

For the flow over the dimple surface Figure 13 shows contours of instantaneous spanwise vorticity at a plane passing through the middle. The boundary layer is initially laminar and remains attached over the first row of dimples. The flow separates close to the third row of dimples forming a shear layer that rolls-up and becomes unstable. The instability of the shear layer is very similar to the one observed by Beratlis *et al.* (2014) for flow over dimpled flat plates and it has been shown that the spanwise oriented vortices give birth to hairpin like structures in a very short distance. As a result of these vortical structures, high-speed flow is transferred towards the wall increasing the momentum near the boundary and delaying separation. As the Reynolds number increases the vortical structures become smaller.

Velocity profiles at three stations along the dimpled surface are shown in Figure 14. The velocity is averaged over time and spanwise direction. Overall the velocity profiles are very similar to each other although the ones for the higher Reynolds number case appear to have more momentum near the wall. As a result the separation point (see Figure 15a), is not affected by the Reynolds number. The

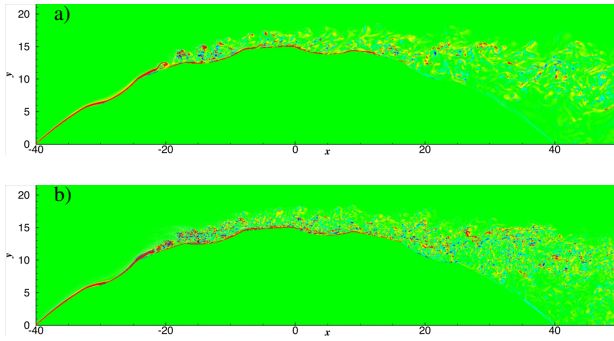


Figure 13. Contours of the instantaneous span wise vorticity at a plane passing through the middle of the dimpled bump. a) $Re_h = 12000$ and b) $Re_h = 30000$

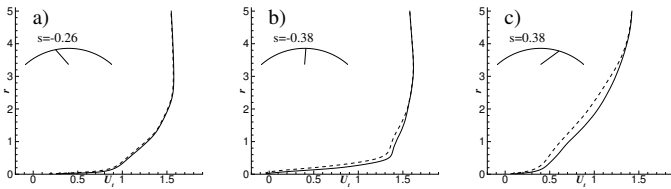


Figure 14. Profiles of the tangential velocity for dimpled bump at different locations: a) $s = -0.26$, b) $s = -0.03$, c) $s = 0.38$, where s is a parameter ranging from -1 at the front to 1 at the rear of the bump. Lines represent: —; $Re = 12000$, - - - $Re = 30000$.

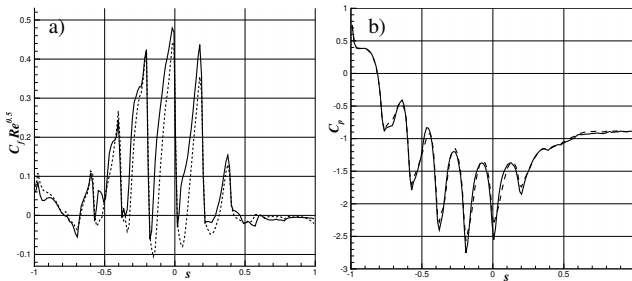


Figure 15. Plots of the ensemble averaged a) skin coefficient C_f normalized by $Re^{0.5}$ and b) pressure coefficient C_p . Lines represent: —; $Re_h = 12000$, - - - $Re_h = 30000$.

skin friction coefficient becomes negative near the stagnation point as the flow separates locally over the dimples. However, global flow separation occurs at $s = 0.6$ for $Re_h = 12000$ and at $s = 0.61$ for $Re_h = 30000$. The pressure coefficient remains unchanged between the two Reynolds numbers, which explains why the drag coefficient remains constant in the post-critical regime.

The turbulent kinetic energy, q , averaged over time and the spanwise direction is shown in Figure 16, and it is plotted along an arc passing 0.5 units above the dimpled surface. Overall the q plots are very similar and it appears that the transition point occurs at the same location for both Reynolds numbers, namely around $s = -0.5$. In particular, the levels of q for the $Re = 30000$ rise a little earlier but farther downstream the levels of q for both cases are in very close agreement with each other. This is a very important observation implying that for the dimpled surface the transition point is very weakly dependent on the Reynolds number. This is contrary to the case of the rough bump where the transition point is strongly dependent on the Reynolds number.

Finally the boundary layer displacement and momentum thick-

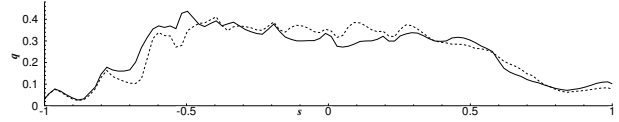


Figure 16. Plot of the unsteady turbulent kinetic energy q averaged over time and span wise direction along an arc passing 0.5 units above the dimpled bump. Lines represent: —; $Re_h = 12000$, - - - $Re_h = 30000$.

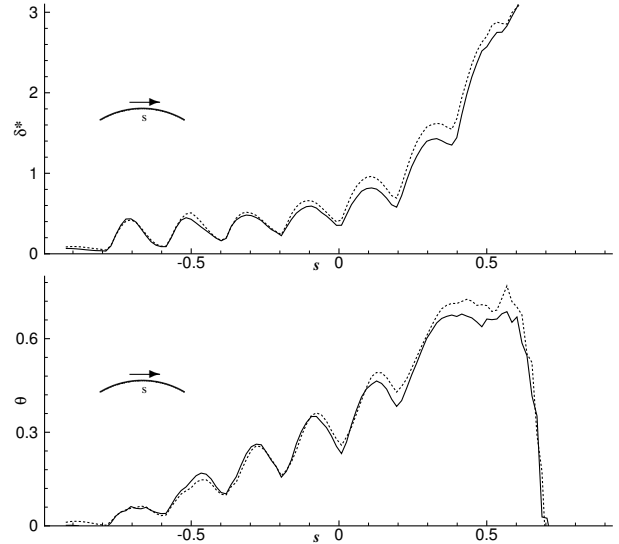


Figure 17. Plot of a) displacement thickness δ^* and b) momentum thickness θ along the dimpled bump. Lines represent: —; $Re = 11000$, - - - $Re = 22000$.

ness are shown in Figure 17. The boundary layer grows in an almost identical way over the first two rows of dimples. As the shear layer becomes unstable over the third row of dimples the boundary layer for the lower Reynolds number case grows a little faster. It appears that with dimples as the Reynolds number increases the boundary layer becomes a little thinner. This is the similar behavior to what happens over a smooth bump and the opposite behavior to the one observed over the rough surface.

CONCLUSION

A series of DNS were performed over a curved boundary with different types of roughness elements. The geometry and boundary conditions are such that the basic physics of the flow over bluff bodies are represented. Two type of roughness elements covering the entire bump were considered: dimples and spherical beads. The study was motivated in part by experiments performed on bluff bodies and the dramatic effect the type of roughness elements have on the drag as a function of the Reynolds number. It is shown that the roughness elements are very efficient in accelerating the drag crisis and reducing the drag compared to the smooth surface at the same Reynolds number. The results are in very good qualitative agreement with experiments of the flow past bluff bodies with dimples and similar roughness.

For the case of the spherical beads the drag is reduced but it rises very quickly as the Reynolds number increases. The dimples on the other hand are able to reduce and maintain the drag at low levels for a large range of Reynolds numbers. A closer look at the evolution of the boundary layer reveals key differences between the two types of roughness elements and their effect on the boundary

layer. For the spherical beads the transition point moves upstream with increasing Reynolds number. As a result, the boundary layer grows thicker much earlier and the flow has less momentum to overcome the adverse pressure gradient. The flow separates earlier with increasing Reynolds number. For the case of the dimpled bump the location of the transition point remains almost fixed with Reynolds number. The boundary layer grows in a very similar fashion and the separation point remains unchanged.

REFERENCES

- Achenbach, Elmar 1971 Influence of surface roughness on the cross-flow around a circular cylinder. *Journal of Fluid Mechanics* **46** (02), 321.
- Achenbach, Elmar 1974 The effects of surface roughness and tunnel blockage on the flow past spheres. *Journal of Fluid Mechanics* **65** (1), 113–125.
- AOKI, Katsumi, MUTO, Koji & OKANAGA, Hiroo 2012 Mechanism of drag reduction by dimple structures on a sphere. *Journal of Fluid Science and Technology* **7** (1), 1–10.
- Aoki, K., Ohike, A., Yamaguchi, K. & Nakayama, Y. 2003 Flying characteristics and flow pattern of a sphere with dimples. *Journal of Visualization* **6** (1), 67–76.
- Balaras, Elias 2004 Modeling complex boundaries using an external force field on fixed cartesian grids in large-eddy simulations. *Computers & Fluids* **33** (3), 375–404.
- Balaras, Elias & Yang, Jianming 2005 Nonboundary conforming methods for large-eddy simulations of biological flows. *Journal of Fluids Engineering* **127** (5), 851.
- Bearman, P W & Harvey, J K 1976 Golf ball aerodynamics. *Aeronautical Quarterly* **27** (02), 112–122.
- Beratlis, N., Balaras, E. & Squires, K. 2014 Effects of dimples on laminar boundary layers. *Journal of Turbulence* **15** (9), 611–627.
- Choi, Jin, Jeon, Woo-Pyung & Choi, Haecheon 2006 Mechanism of drag reduction by dimples on a sphere. *Physics of Fluids* **18** (4), 041702.
- Güven, O., Farell, C. & Patel, V. C. 1980 Surface-roughness effects on the mean flow past circular cylinders. *Journal of Fluid Mechanics* **98** (04), 673.
- Yang, Jianming & Balaras, Elias 2006 An embedded-boundary formulation for large-eddy simulation of turbulent flows interacting with moving boundaries. *Journal of Computational Physics* **215** (1), 12–40.